AGU ADVANCING EARTH AND SPACE SCIENCE

Water Resources Research

RESEARCH ARTICLE
10.1029/2022WR032721

Heterogeneity in Spatiotemporal Variability of High Mountain Asia's Runoff and Its Underlying Mechanisms

Yanxin Zhu[1,2,3], Yan-Fang Sang[1,3,4,5], Bin Wang[6], Arthur Lutz[7], Shi Hu[1,3], Deliang Chen[8], and Vijay P. Singh[9,10]

[1]Key Laboratory of Water Cycle and Related Land Surface Processes, Institute of Geographic Sciences and Natural Resources Research, Chinese Academy of Sciences, Beijing, China, [2]Department of Environmental Systems Science, ETH Zürich, Zürich, Switzerland, [3]University of Chinese Academy of Sciences, Beijing, China, [4]Yarlung Zangbo Grand Canyon Water Cycle Monitoring and Research Station, Tibet Autonomous Region, Linzhi, China, [5]Key Laboratory of Compound and Chained Natural Hazards Dynamics, Ministry of Emergency Management of China, Beijing, China, [6]Department of Atmospheric Sciences, School of Ocean and Earth Science and Technology, International Pacific Research Center, University of Hawaii at Manoa, Honolulu, HI, USA, [7]Department of Physical Geography, Faculty of Geosciences, Utrecht University, Utrecht, The Netherlands, [8]Regional Climate Group, Department of Earth Sciences, University of Gothenburg, Gothenburg, Sweden, [9]Department of Biological and Agricultural Engineering, Zachry Department of Civil and Environmental Engineering, Texas A&M University, College Station, TX, USA, [10]National Water and Energy Center, UAE University, Al Ain, UAE

Key Points:

- Significant runoff variability at interannual and multidecadal timescales is detected in west and central High Mountain Asia (HMA)
- HMA's runoff variability is primarily controlled by precipitation, while catchment properties regulate precipitation effect in diverse ways
- Spatiotemporal variability in HMA's runoff is modulated by large-scale atmospheric drivers including El Niño-Southern Oscillation, Interdecadal Pacific Oscillation, and Atlantic Multidecadal Oscillation

Supporting Information:

Supporting Information may be found in the online version of this article.

Correspondence to:

Y.-F. Sang,
sangyf@igsnrr.ac.cn;
sunsangyf@gmail.com

Citation:

Zhu, Y., Sang, Y.-F., Wang, B., Lutz, A., Hu, S., Chen, D., & Singh, V. P. (2023). Heterogeneity in spatiotemporal variability of High Mountain Asia's runoff and its underlying mechanisms. *Water Resources Research*, *59*, e2022WR032721. https://doi.org/10.1029/2022WR032721

Received 12 JUL 2022
Accepted 18 JUN 2023

Author Contributions:

Conceptualization: Yanxin Zhu, Yan-Fang Sang
Formal analysis: Yanxin Zhu, Yan-Fang Sang
Investigation: Yan-Fang Sang, Shi Hu, Deliang Chen
Methodology: Yan-Fang Sang, Arthur Lutz
Supervision: Yan-Fang Sang, Bin Wang, Deliang Chen
Validation: Yanxin Zhu, Yan-Fang Sang, Bin Wang
Writing – original draft: Yanxin Zhu
Writing – review & editing: Yan-Fang Sang, Bin Wang, Deliang Chen, Vijay P. Singh

Abstract High Mountain Asia (HMA) is the headwater area for major Asian rivers, providing a vast amount of freshwater to billions of people in Asia. These rivers also make their surrounding areas highly vulnerable to destructive water-related disasters. However, the complex spatiotemporal variability of runoff over HMA and its underlying mechanisms are poorly understood. This study investigates into the spatial heterogeneity of HMA's runoff variability at three timescales (interannual, interdecadal, and multidecadal) and the roles played by climate conditions and catchment properties. We find significant interannual and multidecadal variability of runoff in west and central HMA, and significant interdecadal variability in central and east HMA. At interannual and multidecadal timescales, the runoff variability tends to be more significant in dryer basins. The variability of runoff at the three timescales is largely controlled by climate variations, especially precipitation. The catchment properties, including groundwater storage and glacier-snow meltwater, also play important roles in regulating the effect of precipitation. In particular, the high contributions of glacier-snow meltwater in east HMA can weaken the response of runoff variability to precipitation at interannual and multidecadal timescales. The space-time patterns of runoff variability over HMA are driven by atmospheric drivers including El Niño-Southern Oscillation, Interdecadal Pacific Oscillation, and Atlantic Multidecadal Oscillation across timescales. The results of this study provide a better understanding of HMA's runoff variability and its physical mechanisms, which have critical implications for sustainable freshwater management and effective risk mitigation in this densely populated and ecologically vulnerable region.

1. Introduction

High Mountain Asia (HMA), including the Tibetan Plateau (TP) and its surrounding mountain ranges, is the origin of several major Asian rivers, such as the Brahmaputra River, Salween River, Mekong River, Yangtze River, and Yellow River. HMA is also known as the "Asian water tower," providing massive amounts of freshwater to the local inhabitants, agriculture, and industry in the region (Immerzeel et al., 2010, 2020). However, the areas along the rivers are highly vulnerable to destructive natural hazards, like floods, landslides, and mudslides, which threaten people's lives and properties, environment, and ecosystems in the region (Cui & Jia, 2015; Dilley, 2005). Understanding the spatiotemporal variability of hydroclimate and its underlying mechanisms, especially that of runoff, is critical for sustainable freshwater management and effective risk mitigation of climate-related hazards in this densely populated and ecologically vulnerable region.

HMA is mainly influenced by the Asian summer monsoon system and midlatitude westerlies, interacting with the complex topographic features and geographic conditions (Dong et al., 2016; T. Yao et al., 2019). The hydroclimate in this region exhibits significant spatial and temporal variations (Curio & Scherer, 2016; Lai et al., 2021; Sang et al., 2016). However, our current understanding of these variations remains inadequate. Moreover, due to

the high topography, long-term hydroclimatic observations are barely available over HMA, making hydroclimatic studies extraordinarily challenging (A.Wang & Zeng, 2012).

Based on the limited hydrological observations over HMA, previous studies mainly focused on the linear trends in annual, seasonal, and monthly runoff (Tang et al., 2019). They reported that changes in climate and cryosphere have caused significant shifts in the timing and magnitude of runoff over HMA, along with significant spatial heterogeneity due to different runoff compositions, climate influences, and catchment properties (Cuo et al., 2014; Y. Wang et al., 2021). Apart from trend, the periodic variability of runoff at interannual, interdecadal, and longer timescales is also important for freshwater management and mitigation of water-related hazards in HMA (B. Wang et al., 2015; T. Yao et al., 2019). However, this issue was received little attention.

Many studies in the United States, Europe, and Australia have analyzed runoff variability at the basin scale (Gudmundsson et al., 2011; Rice et al., 2016; Xu et al., 2013) and have reported that climate conditions interact with catchment properties, controlling the variability of runoff at multi-timescales as well as its spatial manifestation (Carrillo et al., 2011; Sawicz et al., 2011; T. Zhang et al., 2019; X. Zhang et al., 2019). In particular, the variability of runoff at interannual and longer timescales is governed by climate conditions manifested by the relative availability of precipitation (P) and potential evapotranspiration (E_0), as further performed by the aridity index (P/E_0) (Budyko, 1974; Fu, 1981; H. Yang et al., 2008; L. Zhang et al., 2001). Besides, the variability of runoff tends to be stronger in drier areas (Berghuijs & Woods, 2016).

Furthermore, catchment properties play an indirect but important role in determining how runoff in the basins responds to changes in climatic conditions (Liu et al., 2019; Rice et al., 2015). Basin topography and morphology (e.g., elevation, slope, basin area, and form factor) are known to influence the event-scale hydrological processes, controlling the rainfall-runoff response and routing of water through the watershed channel network (Rice et al., 2016). Some studies have indicated that the catchment properties are related to the runoff supplies (e.g., groundwater storage, glacier, and snow meltwater), which tends to modulate long-term runoff variability through multi-timescale interactions in different runoff components (Gudmundsson et al., 2011; Istanbulluoglu et al., 2012; Xu et al., 2013).

However, HMA's runoff variability at interannual and longer timescales is complicated by climate conditions and unique catchment properties, including diverse topography, morphology, vegetation, soil, and groundwater storage (Cuo et al., 2019). More importantly, HMA has the world's largest glaciers and snow cover outside the polar regions, and rivers originating from the region are most meltwater-dependent, which generate multi-runoff compositions (Khanal et al., 2021). Precipitation supplies 40%–60% of total annual runoff in this region (Lutz et al., 2014), while contributions from baseflow and melting water of glacier-snow cannot be ignored (Cuo et al., 2014; Y. Wang et al., 2021). In the Yarlung Tsangpo River basin (the portion of Brahmaputra River within China), baseflow accounts for 30%–50% in the tributaries like Lhasa River and Nianchu River; and the meltwater feeds 35%–50% to the Niyang River and the upper reach of the Yarlung Tsangpo River (Lutz et al., 2014; Y. Yao et al., 2021). Likewise, in the Salween and Mekong River basins, baseflow and meltwater contribute about 20% and 30%–35% to runoff in their upper reaches, respectively (L. Zhang et al., 2013; Q. Zhao et al., 2019). The large difference in runoff compositions over HMA may increase the spatial heterogeneity of runoff variability in the region. The above explanation indicates the direction for exploring physical causes of spatial and temporal variability of runoff at multi-timescales in the HMA region.

The objective of this study therefore is to investigate the spatial and temporal variability of runoff over HMA and its underlying mechanisms. We mainly concern the Brahmaputra, Salween, and Mekong rivers in this region and focus on three timescales (interannual, interdecadal, and multidecadal). We proceed as follows. Sections 2 and 3 describe data and methods used in this study, respectively. In Section 4, spatial heterogeneity in runoff variability at the three timescales is detected, and its response to climate conditions and catchment properties is examined. In Section 5, the underlying mechanisms behind the space-time patterns in runoff variability are discussed by considering large-scale atmosphere-ocean interactions. Finally, conclusions are given in Section 6.

2. Study Area and Data

This study concerns the Brahmaputra, Salween, and Mekong River basins in HMA (Figure 1). These basins are primarily influenced by the South Asian summer monsoon (SASM) (Cherchi et al., 2011; P. X. Wang et al., 2017; T. Yao et al., 2013). Every year, the SASM brings large amounts of warm and humid moist air from the Indian

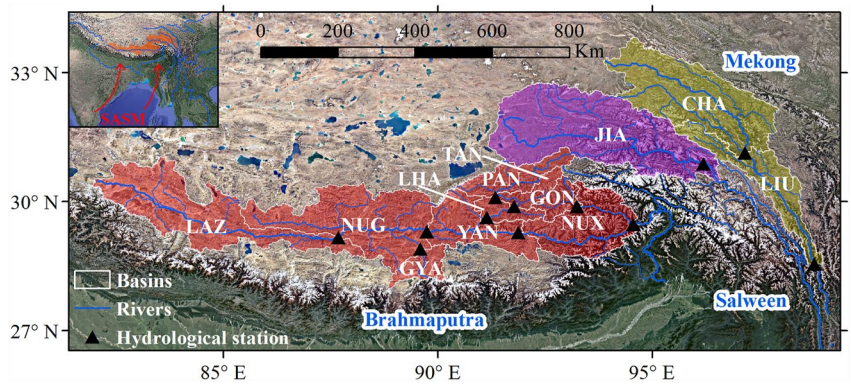

Figure 1. Locations of 12 basins over High Mountain Asia considered in this study. The 12 basins are Lazi (LAZ), Gyantse (GYA), Nugesha (NUG), Pangduo (PAN), Tangjia (TAN), Lhasa (LHA), Yangcun (YAN), Gongbujiangda (GON), Nuxia (NUX), Jiayuqiao (JIA), Changdu (CHA), and Liutongjiang (LIU) from west to east of the region. The red, purple, and yellow zones represent the Brahmaputra, Salween, and Mekong River basins, respectively. The red arrows denote the South Asian summer monsoon.

Ocean into the inland of HMA, accounting for more than 60% of the annual precipitation (Sang et al., 2016). From the northwest to the southeast, the annual precipitation ranges from about 300 mm to more than 2,000 mm, and vegetation varies from alpine meadow, shrub, and grassland to conifer and broadleaf forest. The average elevation of HMA is over 4,000 m, and the terrain is extremely varied. Extensive glaciers and snow cover about 4,200 km^2 (1.2% of this region). The three rivers of concern here contribute about 230 billion m^3 annual discharge to this region and downstream in South and Southeast Asia, which is critical for water security in this area (L. Wang et al., 2021).

Considering the data availability, we use the annual streamflow observations at 12 hydrological stations (Figure 1) for the period of 1961–2010 to detect multi-timescale variability of runoff and its spatial heterogeneity in HMA. There are weak anthropogenic effects, such as land cover change and hydraulic engineering structures, on runoff variability in this region during the period of concern (L. Wang et al., 2021). The DEM (Digital Elevation Model) data from SRTM (Shuttle Radar Topography Mission) at a 90 m spatial resolution was employed to delineate the upstream area of each hydrological station (Jarvis et al., 2008). Correspondingly, the 12 basins include the Lazi (LAZ), Gyantse (GYA), Nugesha (NUG), Pangduo (PAN), Tangjia (TAN), Lhasa (LHA), Yangcun (YAN), Gongbujiangda (GON), Nuxia (NUX), Jiayuqiao (JIA), Changdu (CHA), and Liutongjiang (LIU) from west to east of the region. The runoff (Q) from each basin was computed by excluding the runoff magnitude from the upstream.

Due to limited meteorological observations for all the basins, the APHRODITE (Asian Rainfall Highly-Resolved Observational Data Integration Towards Evaluation of Water Resources) data for the period of 1961–2010 was used for this study. It is a grid-based daily precipitation product that contains a dense network of rain gauges for the whole of Asia (Yatagai et al., 2012), which adequately describes the temporal and spatial variations of precipitation in HMA (Lutz et al., 2014; Tong et al., 2014), especially in the southwest boundary area (Zhu et al., 2020; Zhu & Sang, 2018). Besides, the grid-based meteorological data sets from CMA (China Meteorological Administration) (Y. F. Zhao & Zhu, 2015) were used to estimate annual potential evapotranspiration during 1961–2010 in HMA by the Penman-Monteith formula. The meteorological data sets from CMA were released after strict quality control, including internal temporal and spatial consistency checks, homogeneity tests, and potential outlier detection, which is regarded as one of the most credible meteorological data sets in the study area (Q. Zhao et al., 2019; Y. F. Zhao & Zhu, 2015). The basic climate conditions of each basin were characterized by the mean annual precipitation (P), potential evapotranspiration (E_0), temperature (T), and aridity index (P/E_0), and they were used to examine the influence of climate conditions on the variability of runoff in HMA.

To evaluate the influence of catchment properties on runoff variability, we estimated the basin area, Compound Topographic Index (CTI), mean and standard deviation of elevation, mean and standard deviation of slope, form factor, runoff (Q), runoff coefficient (Q/P), the percentage of sandy soil, the percentage of forest and grassland cover, and the percentage of glacier-snow area of the 12 basins from the SRTM DEM data, Harmonized World

Soil Database (HWSD) (Fischer et al., 2008), and land use products (Xu et al., 2018). Among them, the CTI is a function of basin area and slope:

$$\mathrm{CTI} = \ln(\alpha/\tan\beta), \tag{1}$$

where α represents the basin area, and β refers to the slope. The CTI is strongly correlated with groundwater storage that is also involved in the catchment properties (Moore et al., 1991; Y. Yao et al., 2021). High CTI represents a large basin area and gentle slope or plain, while low CTI represents a small basin area and steep slope or hill. The form factor is defined as the ratio of basin area to the square of basin perimeter l (Horton, 1932):

$$\mathrm{Form\,Factor} = \alpha/l^2. \tag{2}$$

It decreases with the increasing basin area, representing a longer and narrower basin. The above climate conditions and catchment properties of the 12 basins are listed in Table 1.

We also used the monthly mean atmospheric circulation data from the European Centre for Medium-Range Weather Forecasts reanalysis (ERA5) and sea surface temperature (SST) data from NOAA Extended Reconstructed Global SST version 5 (ERSSTv5) covering the period 1961–2010, to examine the large-scale atmospheric drivers of spatiotemporal variability of runoff over HMA.

3. Methods

3.1. Runoff Composition Estimation

We used runoff simulation results obtained from the Spatial Processes in Hydrology (SPHY) model to evaluate the average runoff composition in the 12 basins of HMA (Lutz et al., 2014). The SPHY model is a fully distributed, high-resolution cryosphere-hydrological model, including all important hydro-cryospheric processes, and can operate at flexible spatial scales (sub-basin, basin, and regional). This model was run at a daily time step and at 1×1 km spatial resolution covering the 12 basins, and is capable of simulating the magnitude and composition of runoff in HMA. In this model, the rainfall runoff was calculated as surface runoff from liquid precipitation and lateral flow released from the soil water storage; baseflow was calculated as groundwater flow released from the shallow aquifers; and the glacier-snow runoff was calculated as the glacier melt generated in the glacierized cell fraction and snow melt released from snow storage. More details of the model can be found in Lutz et al. (2014) and Terink et al. (2015). Based on simulation results, we obtained the contribution ratios of rainfall runoff, baseflow, and glacier-snow melt to the total runoff in the 12 basins (see Table 1).

Previous studies have been devoted to identifying different runoff compositions in HMA using environmental isotope tracing methods, digital filter methods or hydrological model simulations (Khanal et al., 2021; Lutz et al., 2014). To confirm the reliability of average runoff composition results from the SPHY model, we compared them with the results of previous study (see Table S1 in Supporting Information S1). The average runoff compositions at the outlets of the Brahmaputra, Salween, and Mekong River basins, as well as most subbasins in HMA, estimated by the SPHY model were similar to the results of the isotope tracing method and digital filter method. Thus, it is deemed that the average runoff compositions in the 12 basins estimated by the SPHY model are reasonable and feasible, based on which we further analyzed their potential influence on runoff variability at the three timescales of concern.

3.2. Discrete Wavelet Spectrum Method

The discrete wavelet spectrum (DWS) method was applied to identify and evaluate the multi-timescale hydroclimatic variability in the study area. This method first decomposes the original time series into components with different timescales through the discrete wavelet decomposition, and then quantifies the significance of these components by using the variance concept. The specifics of the DWS method are described as follows.

The discrete wavelet transform (DWT) of a time series $f(t)$ is expressed as (Wickerhauser, 1996):

$$W_f(j,k) = \int_{-\infty}^{+\infty} f(t)\psi_{j,k}{}^{*}(t)dt \quad \text{with} \quad \psi_{j,k}(t) = {a_0}^{-j/2}\psi\left({a_0}^{-j}t - b_0k\right), \tag{3}$$

Water Resources Research

10.1029/2022WR032721

Table 1
Climate Conditions and Catchment Properties of the 12 Basins of High Mountain Asia (HMA)

		Catchment properties															Climate conditions			
Region	Basin	Area (km^2)	CTI	Elevation (m)	Std-elevation (m)	Slope (°)	Std-slope (°)	Form factor	Q (mm)	Q/P	Sandy soil	Vegetation cover	Glacier-snow cover	Rainr	Baser	GSr	P (mm)	E0 (mm)	P/E_0	T (°C)
West HMA	LAZ	52335.80	6.67	5084.18	406.80	10.03	7.93	0.05	100.08	0.35	0.62	0.87	0.017	0.29	0.12	0.59	287.94	875.13	0.33	−2.59
	GYA	7258.66	6.63	4939.72	378.48	12.16	8.10	0.11	86.03	0.27	0.60	0.87	0.032	0.52	0.18	0.30	318.07	878.37	0.36	−0.55
	NUG	50488.50	6.58	4933.11	501.26	13.88	8.42	0.08	206.01	0.68	0.59	0.86	0.004	0.61	0.25	0.14	303.55	867.07	0.35	−0.92
Central HMA	PAN	13701.60	6.59	5009.18	354.20	14.82	9.40	0.09	470.69	1.06	0.57	0.70	0.013	0.41	0.31	0.28	442.32	808.62	0.55	−1.04
	TAN	6112.51	6.55	4932.10	378.67	16.63	9.04	0.10	239.32	0.52	0.56	0.70	0.001	0.42	0.38	0.21	464.39	813.51	0.57	−0.93
	LHA	6545.32	6.58	4564.32	517.02	15.62	9.00	0.12	228.87	0.58	0.54	0.81	0.001	0.64	0.26	0.11	396.86	868.48	0.46	1.86
	YAN	23016.20	6.58	4693.21	574.03	15.39	8.92	0.09	180.50	0.53	0.56	0.80	0.015	0.62	0.20	0.18	340.15	883.07	0.39	1.51
East HMA	GON	6621.68	6.50	4940.37	435.73	20.72	9.34	0.12	572.16	1.15	0.59	0.63	0.036	0.37	0.29	0.34	498.87	790.43	0.63	−0.96
	NUX	29289.10	6.52	4500.36	599.78	20.96	9.90	0.13	891.33	1.79	0.53	0.68	0.025	0.48	0.21	0.31	499.29	839.67	0.59	2.45
	JIA	76604.60	6.59	4762.42	359.98	13.40	9.37	0.10	330.36	0.65	0.52	0.76	0.014	0.41	0.24	0.35	511.03	786.70	0.65	−2.03
	CHA	52919.70	6.55	4554.37	367.79	13.89	7.98	0.10	281.77	0.56	0.51	0.89	0.004	0.41	0.23	0.36	506.26	774.42	0.65	−2.90
	LIU	23879.20	6.52	4352.48	532.39	17.85	9.17	0.05	293.41	0.60	0.50	0.83	0.002	0.53	0.21	0.27	492.91	823.48	0.60	0.69

Note. CTI, compound topographic index; Q, mean annual runoff depth; P, mean annual precipitation; Rainr, the contribution of rainfall runoff to total runoff; Baser, the contribution of baseflow to total runoff; GSr, the contribution of glacier-snow melt to total runoff; E_0, mean annual evapotranspiration; T, mean annual temperature; P/E_0, mean annual aridity index.

where $\psi(t)$ is the given mother wavelet, with its complex conjugate $\psi^*(t)$ (Strang & Nguyen, 1996); a_0 and b_0 are constants that define the shape of $\psi(t)$, and $W_f(j,k)$ is the discrete wavelet coefficient under the decomposition level j (i.e., timescale $a_0{}^j$) and time position k. The dyadic DWT, with $a_0 = 2$ and $b_0 = 1$, is widely used for hydroclimatic time series analysis (Agarwal et al., 2017):

$$W_f(j,k) = \int_{-\infty}^{+\infty} f(t)\psi_{j,k}{}^*(t)dt \quad \text{with} \quad \psi_{j,k}(t) = 2^{-j/2}\psi\left(2^{-j}t - k\right). \tag{4}$$

In the first decomposition step, the result includes two coefficient sets as "detail" (D) and "approximation" (A). In the residual steps, only the approximation coefficients are analyzed. The component $f_j(t)$ under each level j ($j = 1, 2, \ldots, M$) is reconstructed as:

$$f_j(t) = \sum_k W_f(j,k)\psi^*\left(2^{-j}t - k\right). \tag{5}$$

The highest decomposition level M depends on the data length L of time series $f(t)$: $M = \log_2(L)$. Thus, there are $M + 1$ components for the original time series $f(t)$, with two components ($f_{M\_D}(t)$ and $f_{M\_A}(t)$) at the highest-level M. Note that the component $f_{M\_A}(t)$ at the highest decomposition level is the monotonic trend; the D components at other decomposition levels, except the first one, are referred to as periodic oscillations (Gudmundsson et al., 2011; Sang et al., 2018). The D component at the first decomposition level exhibits high-frequency variations and is generally regarded as the stochastic component of the original time series.

Then, the variance $E(j)$ of each component $f_j(t)$ was calculated to establish DWS:

$$E(j) = \mathrm{var}(f_j(t)). \tag{6}$$

Sang (2012) found that the DWS of diverse types of noise data strictly followed the same exponentially declining rule as timescale increased, and it obviously differs from that of hydroclimatic time series which usually include some significant signals at multi-timescales. Thus, the DWS of noise data can be defined as the reference DWS (RDWS), whose confidence interval (CI) can be estimated by the Monte-Carlo (MC) experiments (Sang et al., 2021). By comparing the DWS of hydroclimatic time series with the RDWS and its CI, the statistical significance of the variability at different timescales in the former can be evaluated.

The DWS method has been widely applied to detect the hydroclimatic variability at different timescales; moreover, as a uniform RDWS is used in the method, it is favorable to investigate the spatial heterogeneity of hydroclimatic variability. In this study, we used this method to detect the spatiotemporal variability of runoff, as well as the climate conditions including P, E_0, P/E_0, and T at interannual, interdecadal, and multidecadal timescales in HMA. Given the data length of 50 years (1961–2010) of runoff, the D components at the 2nd and 3rd decomposition levels reflect the interannual variability (2–8 years); the D component at the 4th decomposition level reflects the interdecadal variability (about 16 years); and the D and A components at the 5th decomposition level are mainly controlled by the climate mode at multidecadal and even larger timescales, which is called as "multidecadal variability" (about 32 years) in this study. To be specific, if the variance of certain components is above the CI (95% confidence level is concerned in this study), the variability at the corresponding time scale is regarded as statistically significant.

Moreover, regression analysis was employed to examine the influence of climate conditions and catchment properties (see Table 1) on the variability of runoff at the above three timescales.

3.3. Atmospheric Teleconnection Diagnosis

To investigate the potential atmospheric drivers of space-time patterns in runoff variability at the three timescales, we calculated the correlations between the decomposed runoff timeseries (interannual, interdecadal, and multidecadal timescales) and climate indices (i.e., El Niño-Southern Oscillation (ENSO), Interdecadal Pacific Oscillation (IPO), and Atlantic Multidecadal Oscillation (AMO)). Furthermore, the decomposed runoff timeseries at the three timescales were regressed onto the anomalies of SST and 500 hPa wind fields, as well as onto the geopotential height (GHT) and wind fields at 200 hPa, to explore the physical mechanisms of large-scale atmospheric drivers influencing runoff variability in HMA.

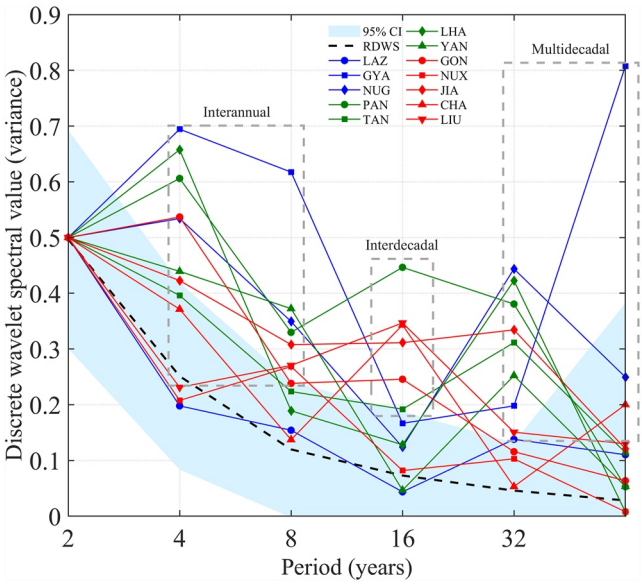

Figure 2. Discrete wavelet spectra of the annual runoff time series at the 12 basins over High Mountain Asia during 1961–2010. The black dashed curve is the reference discrete wavelet spectrum, with its confidence interval (blue band) at the 95% confidence level.

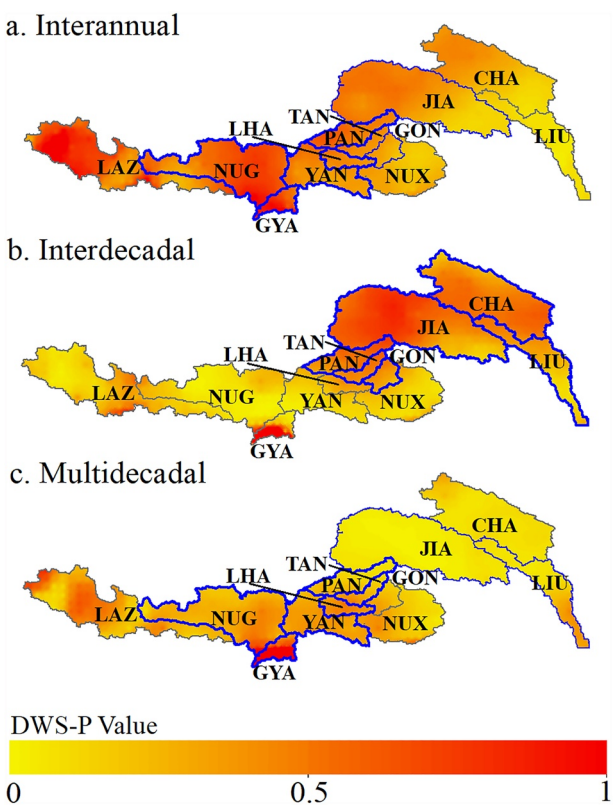

Figure 3. Significance of (a) interannual, (b) interdecadal, (c) multidecadal variability in annual precipitation (shadings: DWS-P value) in the 12 basins in High Mountain Asia. The basins with significant DWS-Q values of runoff at the 95% confidence level are marked in blue outlines here.

For the multidecadal timescale, the eddy GHT anomalies were further used to verify the mid-latitude wave-like pattern, which are defined as the deviation of height anomalies from the zonal mean (Hu, Wu, et al., 2022; Hu, Zhou, et al., 2022). And the wave activity flux (WAF) was used to measure the horizontal propagation of the quasi-stationary Rossby waves (Takaya & Nakamura, 2001). Its horizontal components in pressure coordinates are described as follows:

$$\mathrm{WAF} = \frac{p}{2|U|}\begin{Bmatrix} \overline{u}\left(\phi_x'^2 - \phi'\phi'_{xx}\right) + \overline{v}\left(\phi'_x\phi'_y - \phi'\phi'_{xy}\right) \\ \overline{u}\left(\phi'_x\phi'_y - \phi'\phi'_{xy}\right) + \overline{v}\left(\phi_y'^2 - \phi'\phi'_{yy}\right) \end{Bmatrix} \quad (7)$$

where the quantity $|U|$ is the magnitude of the climatological wind; u and v represents the zonal and meridional wind, respectively; φ is the stream function; and p is the normalized pressure (pressure/1,000 hPa). The overbars and primes denote mean climatology and anomalies, respectively. The subscripts x and y indicate the zonal and meridional gradients, respectively.

4. Results

4.1. Multi-Timescale Variability of Runoff in HMA

The interannual, interdecadal, and multidecadal variability, as well as monotonic trends in the annual runoff observed in the 12 basins in HMA were quantified using the DWS values (denoted as DWS-Q), and their statistical significance was evaluated by comparing with the 95% CI (the blue band in Figure 2). The results in Figure 2 show that the DWS values of annual runoff time series from 4-year to 8-year period are above the 95% CI in the GYA, NUG, PAN, LHA, and YAN basins, thus the periodic oscillations of runoff at interannual timescales are regarded as significant in these basins. While the DWS values of annual runoff time series from 4-year to 8-year period are close to the upper limit of the 95% CI in the TAN, GON, and JIA basins (Figure 2), representing the weaker interannual variability of runoff compared to the above five basins. The high DWS-Q above the 95% CI at 16-year period suggests significant interdecadal variability of runoff in the PAN, TAN, GON, JIA, CHA, and LIU basins, but except the other six basins. Besides, we found that the DWS-Q for about 32-year period is above the 95% CI in the GYA, NUG, TAN, PAN, LHA, and YAN basins, as well as the JIA and LIU basins, indicating significant multidecadal variability of runoff in these basins. Only the GYA basin indicates a significant monotonic trend in runoff, with its last DWS value above the 95% CI. This is consistent with the negative trend identified by the Mann-Kendall test ($Z = -3.22$, Figure S1 in Supporting Information S1).

Based on the DWS values of annual runoff time series in the 12 basins (Figure 2), we further display the spatial distribution of the significance of runoff variability at interannual, interdecadal, and multidecadal timescales. The results in Figure 3 show that the significant interannual variability of runoff is mainly identified in the west and central HMA (GYA, NUG, PAN, TAN, LHA, and YAN basins, see Figure 3a), while the GON and JIA basins in east HMA also exhibit weak runoff variability at the interannual timescale. At the interdecadal timescale, the basins showing significant variability in runoff are mostly located in central and east HMA (PAN, TAN, GON, JIA, CHA, and LIU basins, see Figure 3b). At the multidecadal timescale, the significant runoff variability mainly occurs in west and central HMA (GYA,

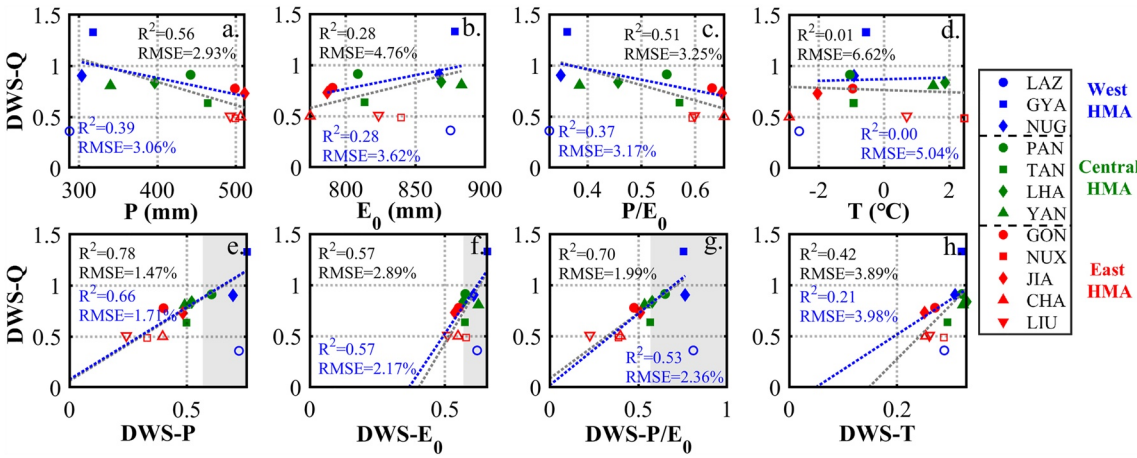

Figure 4. Regression relationships between the discrete wavelet spectral value of the annual runoff (DWS-Q) and climate conditions at the interannual timescale in the 12 basins over High Mountain Asia. The climate conditions include the annual precipitation (P), evapotranspiration (E_0), aridity index (P/E_0), temperature (T), and their discrete wavelet spectral values (denoted as DWS-P, DWS-E_0, DWS-P/E_0, and DWS-T). The scatters in gray areas represent the basins with significant climate variability at 95% confidence level. The filled scatters indicate the basins with significant runoff variability at 95% confidence level, while those basins with insignificant runoff variability are shown in unfilled scatters. The black dotted lines represent the fitting lines between the DWS-Q and the climate conditions of the 12 basins, while the blue dotted lines represent those of the basins with significant runoff variability at 95% confidence level.

NUG, TAN, PAN, LHA, and YAN basins, see Figure 3c), except the JIA and LIU basins, which coincides with the spatial pattern of runoff variability at the interannual timescale.

Following the spatial pattern of runoff variability at the three timescales of concern, HMA can be primarily divided into three sub-regions: west HMA (LAZ, GYA, and NUG basins), central HMA (PAN, TAN, LHA, and YAN basins), and east HMA (GON, NUX, JIA, CHA, and LIU basins). Moreover, we computed the average values of DWS-Q in the west, central and west regions of HMA, respectively. Results in Table S2 in Supporting Information S1 show that there is an increase in the interannual and multidecadal variability of runoff from east, central to west HMA, with a mean DWS-Q value of 0.63, 0.80, and 1.12 at the interannual timescale and that of 0.20, 0.41, and 0.56 at the multidecadal timescale (Table S2 in Supporting Information S1). However, the interdecadal variability of runoff weakens westward over HMA, with mean DWS-Q values of 0.31, 0.20, and 0.15 correspondingly (Table S2 in Supporting Information S1), being consistent with the results in Figure 3.

Overall, the above results indicate that the interannual and multidecadal variability of runoff was significant in west and central HMA, while the interdecadal variability of runoff was significant in east HMA. Moreover, the runoff variability in HMA had an east-west pattern, which gradually strengthened from east, and central to west HMA at the interannual and multidecadal timescales but weakened in the same direction at the interdecadal timescale.

4.2. Influence of Climate Conditions and Catchment Properties on the Runoff Variability in HMA

4.2.1. Influence of Climate Conditions

To examine the climate effect on runoff variability and its spatial pattern at interannual, interdecadal, and multidecadal timescales over HMA, here we analyzed the regression relationships of DWS-Q with eight climate indicators, including the mean value of annual P, E_0, P/E_0, and T, as well as their DWS value (denoted as DWS-P, DWS-E_0, DWS-P/E_0, and DWS-T), and the results are shown in Figures 4–6 corresponding to the three timescales, respectively.

At the interannual timescale (see Figure 4), DWS-Q had a significant negative correlation with P ($R^2 = 0.56$) and P/E_0 ($R^2 = 0.51$), and a weak positive correlation with E_0 ($R^2 = 0.28$, $p > 0.05$) in the 12 basins. It implied that drier basins had greater interannual variability of runoff. In particular, when P was less than about 450 mm, E_0 was more than about 825 mm and P/E_0 was smaller than about 0.55, the interannual variability of runoff tended to be statistically significant, which was typical in the basins of west and central HMA. Moreover, DWS-Q was positively correlated with DWS-P ($R^2 = 0.78$), DWS-E_0 ($R^2 = 0.57$) and DWS-P/E_0 ($R^2 = 0.70$) in the 12 basins,

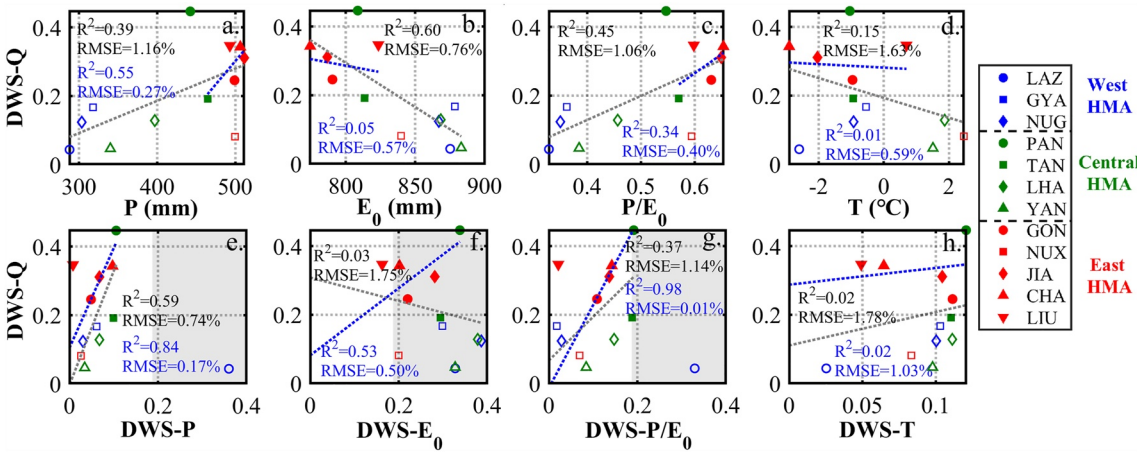

Figure 5. Same as Figure 4, but for the interdecadal timescale.

passing the 5% significance test. As the DWS-P/E_0 was significant (with their DWS values above 95% CI) in most basins of west and central HMA, it caused significant interannual variability of runoff over there. Although significant positive correlations were found between DWS-T and DWS-Q ($R^2 = 0.42$), there was weak correlation ($R^2 = 0.01$) between T and DWS-Q, indicating the weak influence of T on DWS-Q at the interannual timescale.

At the interdecadal timescale (see Figure 5), DWS-Q had a significant positive correlation with P ($R^2 = 0.39$) and P/E_0 ($R^2 = 0.45$), and a significant negative correlation with E_0 ($R^2 = 0.60$) in the 12 basins, being in contrast to that at the interannual timescale. It means that the interdecadal variability of runoff was greater in wetter basins in central and east HMA. Besides, DWS-Q was positively correlated with DWS-P ($R^2 = 0.59$) and DWS-P/E_0 ($R^2 = 0.37$) in the 12 basins, passing the 5% significance test. DWS-P and DWS-P/E_0 were greater in most basins of central and east HMA than that in west HMA, causing significant interdecadal variability of runoff in the former. Additionally, both T and its DWS value (i.e., DWS-T) had no significant correlation with DWS-Q at the interdecadal timescale in the 12 basins, implying the weak influence of temperature.

At the multidecadal timescale (see Figure 6), the correlations between DWS-Q and these climate indicators were similar as those at the interannual timescale. DWS-Q was negatively correlated with P ($R^2 = 0.61$) and P/E_0 ($R^2 = 0.62$), and positively correlated with E_0 ($R^2 = 0.54$) in the 12 basins. In addition, significant positive correlations between DWS-Q and DWS-P ($R^2 = 0.82$), DWS-E_0 ($R^2 = 0.74$), and DWS-P/E_0 ($R^2 = 0.81$) were also found in the 12 basins, with their large values corresponding to significant multidecadal variability of runoff in the most basins of west and central HMA. Although DWS-T and DWS-Q had significant correlations ($R^2 = 0.63$),

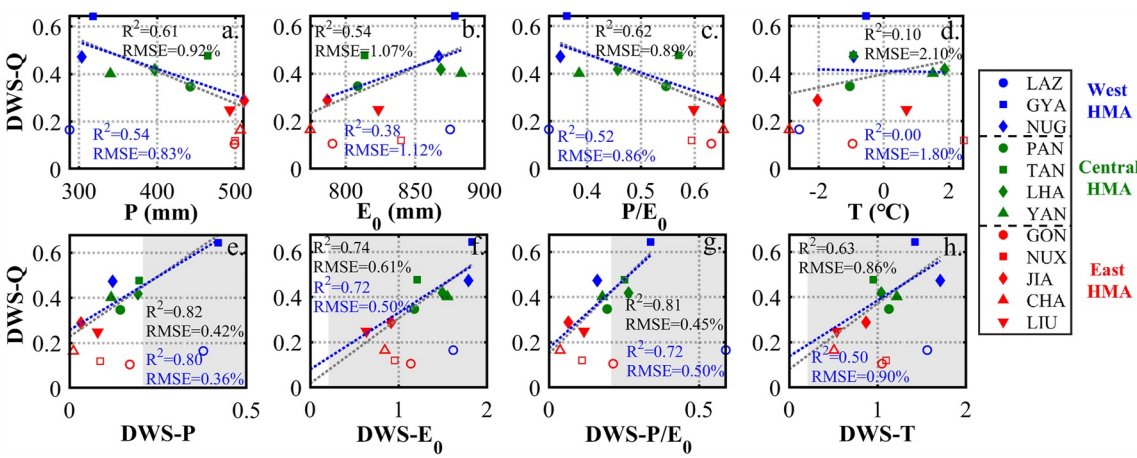

Figure 6. Same as Figure 4, but for the multidecadal timescale.

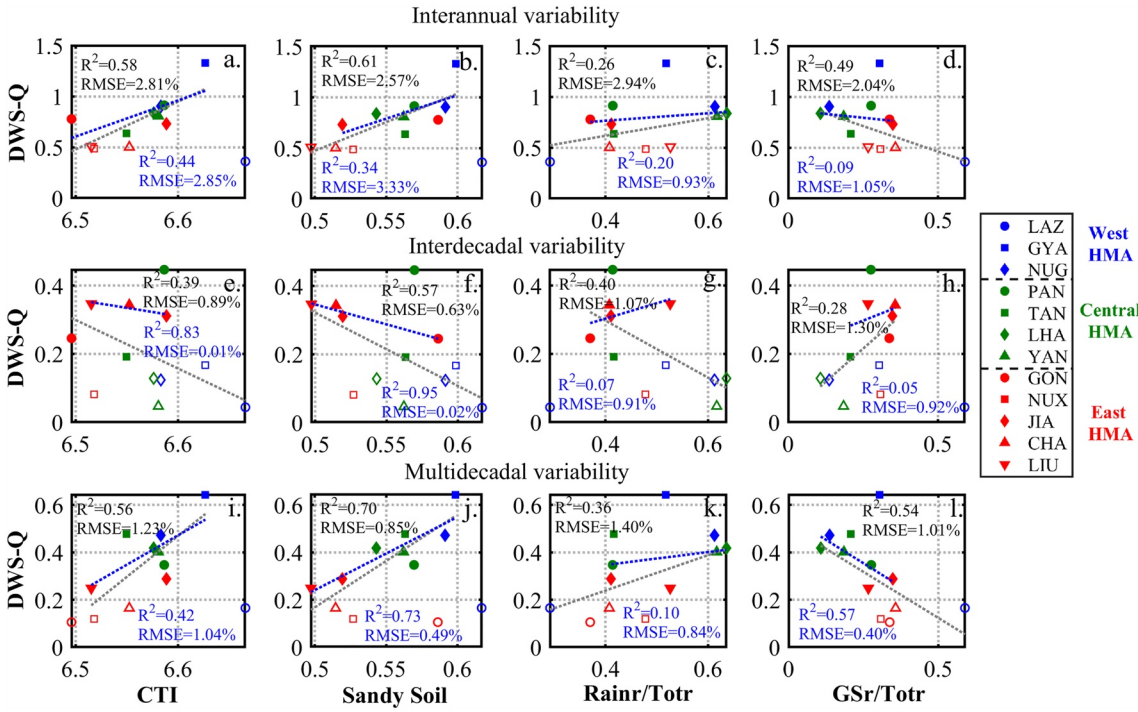

Figure 7. Regression relationships between the discrete wavelet spectral value of the annual runoff (DWS-Q) and catchment properties at (a–d) interannual, (e–h) interdecadal, and (i–l) multidecadal timescales in the 12 basins over High Mountain Asia. The catchment properties include the Compound Topographic Index, the percentage of sandy soil area (Sandy Soil), the contributions of rainfall runoff (Rainr/Totr) and glacier-snow melt (GSr/Totr) to the total runoff. The filled symbols indicate the basins with the significant runoff variability at 95% confidence level, while those basins with insignificant runoff variability are shown as unfilled symbols. The black dotted lines represent the fitting lines between the DWS-Q and the catchment properties of the 12 basins, while the blue dotted lines represent those of the basins with significant runoff variability at 95% confidence level.

insignificant relationship (R^2 = 0.10) between T and DWS-Q caused the weak influence of temperature on the multidecadal variability of runoff over HMA.

For the long-term trend, a significant positive correlation of DWS-Q with DWS-P (R^2 = 0.66) and DWS-P/E_0 (R^2 = 0.48) was found here, but the DWS-Q had no significant correlations with P and P/E_0 (Figure S2 in Supporting Information S1). This suggested that the monotonic trends in runoff were more influenced by the variability of climate conditions rather than its climatology.

From the above results, it was found that drier basins exhibited more significant interannual and multidecadal variability of runoff, but the runoff variability at interdecadal timescale was more significant in wetter basins in HMA. This result supports the universal phenomenon across the globe (Berghuijs & Woods, 2016; Carmona et al., 2014). Moreover, the runoff variability at the three timescales of concern was closely related to the variability of climate conditions, especially precipitation (Figure 3). Comparatively, the variability of runoff was stronger than that of precipitation for the three timescales, with about 1% variability in P and P/E_0 corresponding to 1.5%–2.5% variability in runoff in HMA, which is consistent with the findings of previous studies (Sang et al., 2020; Sankarasubramanian & Vogel, 2003).

4.2.2. Influences of Catchment Properties

Here we employed 15 indicators to investigate the relationships between runoff variability and catchment properties in HMA. They were the logarithmic basin area, CTI, elevation, standard deviation of elevation, slope, standard deviation of slope, form factor, runoff (Q), runoff coefficient (Q/P), the percentage of sandy soil, the percentage of forest and grassland cover, the percentage of glacier-snow area, and the contributions of rainfall runoff, baseflow, and glacier-snow melt to the total runoff (see Table 1). The correlations between runoff variability (DWS-Q) and these 15 indicators at the three timescales are shown in Figure 7.

A significant positive correlation was found between DWS-Q and CTI and the percentage of sandy soil at the interannual and multidecadal timescales in the 12 basins (Figure 7). Several studies have demonstrated that the catchment properties (e.g., topography, soil properties) determine the groundwater levels (Bachmair & Weiler, 2012; Moore et al., 1991; Rinderer et al., 2014). Large drainage area and gentle slope (as described by high CTI) and high soil infiltration capacity (as described by high percentage of sandy soil) is favorable for large groundwater storage. The groundwater storage preserves a climate memory in the hydrologic system and usually behaves a multi-year oscillation (Gudmundsson et al., 2011). Increasing groundwater storage is associated with strengthened low-frequency variability, which explains high runoff variability at interannual to multidecadal timescales in HMA. As a result, larger groundwater storage could contribute to more significant interannual and multidecadal variability of runoff and overlay the precipitation effects in the basins of west and central HMA. The important role of groundwater in runoff variability was also recognized by previous studies (Istanbulluoglu et al., 2012; H. Wang et al., 2015).

In Figure 7, DWS-Q shows a significant positive correlation with the contribution of rainfall to total runoff (Rainr/Totr) at interannual and multidecadal timescales, being consistent with the precipitation effects on runoff variability discussed in Section 4.2.1. However, there is a significant negative correlation between DWS-Q and the contribution of glacier-snow melt to total runoff (GSr/Totr). The glacier-snow meltwater usually has a longer response time in runoff (J. Wang et al., 2021), which could weaken the runoff response to precipitation, providing the buffering effect to runoff variability. Thus, high contributions of glacier-snow meltwater reduce the runoff variability at interannual and multidecadal timescales in east HMA, and also explain the abnormal weak runoff variability in the LAZ basin, in spite of the high precipitation variability in the area.

At the interdecadal timescale, there is a negative correlation of DWS-Q with the CTI ($R^2 = 0.39$) and the percentage of sandy soil ($R^2 = 0.57$) in the 12 basins in HMA (Figure 7). DWS-Q was negatively correlated with the contribution of rainfall to total runoff (Rainr/Totr) ($R^2 = 0.40$) but positively correlated with the contribution of glacier-snow melt to total runoff (GSr/Totr) ($R^2 = 0.28$) at the interdecadal timescale. In other words, the phenomenon of land surface controls on the runoff variability at the interdecadal timescale, was opposite to that at the interannual and multidecadal timescales. The relationships between mean state of catchment properties and runoff variability are much weaker than that of climate conditions, thus might be misleading at the interdecadal timescale. Further studies need to be done to explain the connections between catchment properties and runoff variability at the interdecadal timescale, by considering the dynamics of groundwater and glacier-snow meltwater.

The relationships between DWS-Q and the other 11 indicators can be found in Figures S3, S4, and S5 in Supporting Information S1. It shows that although CTI is the compound of basin area and slope, the single indicator itself cannot well explain the variability of runoff at the three timescales. The elevation is significantly correlated with DWS-Q at the three timescales (Figures S3, S4, and S5 in Supporting Information S1), but the spatial pattern of the elevation follows that of the climate conditions, suggesting that this correlation may not represent an independent mechanism. The positive correlation between DWS-Q and the contribution of baseflow to total runoff (Baser/Totr) at the three timescales were similar to that about CTI, due to their similar physical mechanisms. The other indicators like form factor and vegetation cover had insignificant correlations with DWS-Q at the three timescales in the 12 basins (Figures S3, S4, and S5 in Supporting Information S1), implying their weak influence on runoff variability.

The above results elaborate the effects of catchment properties, especially the groundwater storage and soil texture, as well as the glacier-snow melt, which can amplify or weaken the climate effects on the variability of runoff at the timescales of concern in this study. Analysis of the influence of climate conditions and catchment properties on runoff variability indicates that climate conditions have a strong and direct influence on the runoff variability at the interannual, interdecadal, and multidecadal timescales, while the catchment properties appear more likely to regulate the runoff variability indirectly via interactions with climate processes within multi-timescales. They provide a deeper insight into the mechanisms for the variability of runoff in HMA.

5. Discussion

5.1. Physical Mechanisms Behind the Runoff Variability in HMA

Many studies have reported the impacts of large-scale atmosphere-ocean modes on precipitation in HMA. At the interannual timescale, the developing ENSO has a significant influence on precipitation variability in the

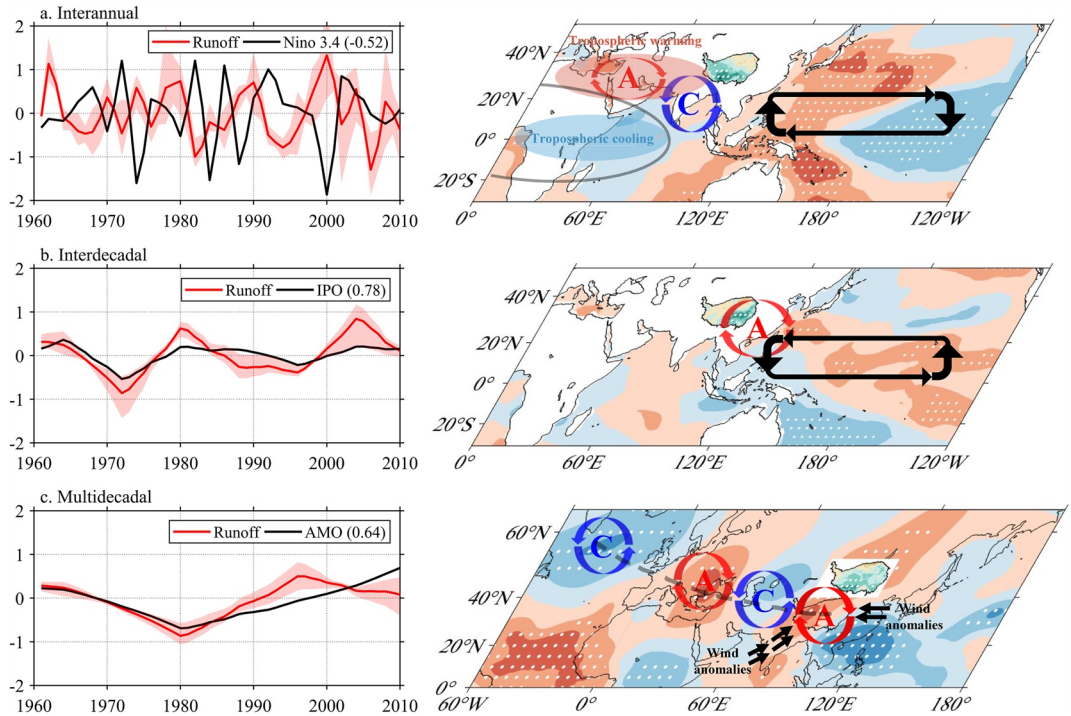

Figure 8. Left: Decomposed time series of area-averaged runoff and corresponding climate indices at the (a) interannual, (b) interdecadal, and (c) multidecadal timescales, respectively. The red band represents the range from minimum to maximum of decomposed runoff time series among the 12 basins in High Mountain Asia (HMA). Their correlation coefficients are shown in parentheses. Right: Schematic of the physical mechanisms responsible for the runoff variability over HMA at the three timescales. The black rectangles with arrows represent the Walker circulation. The red-ringed arrows labeled A denote the anticyclone, while the blue-ringed arrows labeled C indicate the cyclone. The gray solid line represents the Kelvin wave. The gray dashed line represents the propagation path of Rossby waves.

southwestern HMA (Hu et al., 2021; Hu, Wu, et al., 2022), while the precipitation variability over the southeastern HMA is closely associated with the North Atlantic Oscillation (NAO) (Hu, Zhou, et al., 2022; Z. Wang et al., 2017). At the multidecadal timescale, AMO is an important modulator of the shift from dry to wet over the inner HMA around mid-1990s (Sun et al., 2020). Based on the results in this study, the runoff variability at the three timescales is largely controlled by precipitation in HMA (Gudmundsson et al., 2011; Nippgen et al., 2011; T. Yao et al., 2012). However, it remains unclear about the response of runoff variability in HMA to the large-scale atmospheric drivers. The physical mechanisms of their relationship are identified and explained at the following three timescales.

5.1.1. Interannual Timescales

At the interannual timescale, the runoff in HMA is closely associated with ENSO, with a negative correlation coefficient of −0.52 (Left subplot in Figure 8a). Specifically, the correlation map of SST also presents the SST cooling over the equatorial central-eastern Pacific and SST warming over the western Pacific and maritime continent (MC), which is a typical La Niña pattern (Right subplot in Figure 8a). From the 200 hPa circulation fields, the southern HMA is controlled by the South Asian High (SAH), with remarkable positive geopotential and anticyclone anomalies centered at the Arabian Peninsula (the red-ringed arrows in Figure 8a; Figures S6a and S7a in Supporting Information S1). In a La Niña event, the Walker circulation (the black rectangle with arrows in Figure 8a) is strengthened and westward shifted, with the basic physical mechanisms by enhancing the convective heating over the MC and reducing the convective heating over the central-eastern Pacific (B. Wang et al., 2003). On one hand, the suppressed convection over the central-eastern Pacific excites the tropical tropospheric cooling over the Indian Ocean through atmospheric Kelvin wave (the solid gray line in Figure 8a). The upper tropospheric warming over subtropical Eurasia and cooling over the Indian Ocean could further strengthen the SAH, leading to ascending-motion anomalies over HMA, especially in its western region (Figure S8a in Supporting Information S1), and thus contributing to positive anomalies of precipitation and runoff (Hu et al., 2021; Hu,

Wu, et al., 2022). On the other hand, the enhanced convection over the MC stimulates an off-equatorial low-level cyclone (the blue-ringed arrows in Figure 8a) over the Indian Peninsula and the Bay of Bengal, which is also favorable for positive precipitation and runoff anomalies in the western part of HMA through the "up and over" moisture transport mechanism (Dong et al., 2016).

For a developing El Niño (as the anti-phase of La Niña) pattern, the anomalous circulation patterns would cause the opposite changes of precipitation and runoff. Therefore, the phase transition of ENSO at interannual timescale plays a dominant role in the significant interannual variability of precipitation and runoff over the west and central HMA. Comparatively, the east HMA is not sensitive as the west HMA to the circulation anomalies forced by ENSO. Besides, the east HMA is documented to be more linked with the NAO, but with a much lower variance than ENSO. Thus, the interannual variability of precipitation and runoff in the east HMA is less significant than that in the west and central HMA.

5.1.2. Interdecadal Timescales

At the interdecadal timescale, the runoff has a positive correlation with IPO (R^2 = 0.78, Left subplot in Figure 8b). The correlation map of SST presents the positive IPO pattern, with the SST warming over the equatorial central-eastern Pacific and SST cooling over the western Pacific and MC (Right subplot in Figure 8b). And there is positive 200 hPa geopotential and anticyclone anomalies over the western Pacific (Figures S6b and S7b in Supporting Information S1), which is characterized by the subtropical high-pressure system over the western Pacific (WPSH, the red-ringed arrows in Figure 8b). The positive IPO weakens the Walker circulation over the tropical Pacific (the black rectangle with arrows in Figure 8b), by depressing the convective heating over western Pacific and MC, but enhancing the convective heating over the central-eastern Pacific (Dong & Dai, 2015; X. Huang et al., 2020). The suppressed convection over the western Pacific and MC contributes to the development of WPSH (T. Li et al., 2017). Thus, the IPO affects hydroclimate in HMA through modulating in the position and strength of the WPSH (L. Yang et al., 2022; Y. Zhao & Zhou, 2021). During the positive phase of IPO, the WPSH tends to be stronger and farther westward to the southeastern edge of HMA, which promotes the water vapor transport from the Indian Ocean to the central and east HMA, leading to ascending motion and thus increasing precipitation and runoff in this region (Figure S8b in Supporting Information S1). Conversely, during the negative phase of IPO, the WPSH tends to be weaker and farther eastward, resulting in negative anomalies of precipitation and runoff in the region. The IPO is thought to have a significant influence on the interdecadal variability in precipitation and runoff over the central and east HMA.

5.1.3. Multidecadal Timescales

At the multidecadal timescale, there is a significant correlation between the runoff and AMO (R^2 = 0.64, Left subplot in Figure 8c). The correlation map of SST presents the SST warming over the Atlantic Ocean, which is characterized by the positive phase of AMO (Figure S6c in Supporting Information S1). Moreover, the AMO is coupled with the interdecadal Silk Road pattern (the blue and red ringed arrows across the Eurasian continent in Figure 8c), driving the stationary Rossby waves (the dashed gray line across the Eurasian continent in Figure 8c; Figures S6c and S7c in Supporting Information S1) that propagates from the North Atlantic Ocean to downstream East Asia (Sun et al., 2020). The Silk Road pattern-related anomalous cyclone to the western HMA (the blue ringed arrow) could strengthen the SASM winds and promote the water vapor transport from the Arabian Sea into the inner HMA, while the anomalous anticyclone over HMA (the red ringed arrow) could weaken the westerlies and prevent the export of water vapor transport to the east boundary of HMA (Hu & Zhou, 2021). Both the anticyclone and cyclone here are favorable for the ascending motion with positive anomalies of precipitation and runoff over HMA, especially in the western and central HMA (Figure S8c in Supporting Information S1). The opposite would occur in the negative phase of AMO.

The above results provide a deep insight into the physical mechanisms behind the influence of atmospheric drivers on runoff variability over HMA. The runoff variability in this region has a synchronous response with precipitation to the large-scale atmospheric drivers, but presenting significant spatial heterogeneity. At the interannual and multidecadal timescales, the runoff variability in the west HMA is more sensitive to the modulations of ENSO and AMO than the east HMA, respectively. At the interdecadal timescale, IPO has a more powerful effect on the runoff variability in the east HMA. The wetting after 1990s in the west HMA is found to be related to the negative-to-positive AMO phase transitions (Hu & Zhou, 2021; Sun et al., 2020). In the next few decades, if the positive AMO phase persists, the west HMA could keep undergoing a wet climate and increase the potential

flood risks. Whereas, if a negative AMO phase occurs, the west HMA would experience a dry period and face the increasing possibility of droughts. Particularly, the simultaneous effects of ENSO and AMO would greatly enhance the occurrence of extreme events in the west HMA, which should be paid high attention for the climate predictions. Therefore, the roles of atmospheric drivers at different spatial and temporal scales are supposed to comprehensively considered in regulating the hydroclimatic variability over HMA, to optimize climate adaption strategies in this region and downstream areas.

5.2. Uncertainties and Limitations

5.2.1. Data

Long-term hydrometeorological observations are fundamental to understand the historical variability of streamflow. However, the data scarcity over HMA, due to high elevation and harsh environment, makes the streamflow researches extremely challenging (L. Wang et al., 2021). In this study, we obtained the available streamflow observations (at least 50 years) of 12 basins (as shown in Figure 1) in HMA. Although there are some observed streamflow data in other basins of HMA, they are too short (usually shorter than 10 years) to explore long-term runoff variability in HMA.

In some basins like PAN, GON, and NUX, their mean annual values of Q/P (runoff coefficient) are higher than 1. On the one hand, the water budget imbalance in PAN basin could be attributed to the paleo-groundwater discharge through the tensile tectonic belts (near PAN basin) in the middle reach of Yarlung Zangbo River (Tan et al., 2021), while the glacier-snow melt water is an important extra supply to the runoff in GON and NUX basin (Lutz et al., 2014; Y. Wang et al., 2021; Q. Zhao et al., 2019). On the other hand, the mean annual precipitation in NUX basin is likely to be underestimated due to its complex terrain, despite that the APHRODITE data used in this study have been verified to have a good performance in describing the temporal and spatial variations of precipitation over HMA (Yatagai et al., 2012; Zhu et al., 2020). We have compared the Q/P values in these basins using the APHRODITE data with that using some other precipitation data sets, which shows similar results (e.g., Y. Yao et al., 2021).

Even there may have certain uncertainty for Q/P in these basins, it will not influence the main results in this study, as the indicator of Q/P has weak correlation to the runoff variability (as shown in the first sub-Figure in the third row in Figures S3, S4, and S5 in Supporting Information S1), that is, it is not the main factor influencing the runoff variability at interannual and longer timescales in HMA.

5.2.2. Methods

The DWS method was applied to detect and evaluate the spatiotemporal variability of runoff, as well as the climate conditions including P, E_0, P/E_0, and T at interannual, interdecadal, and multidecadal timescales at 12 basins in HMA. We found significant interannual and multidecadal variability of runoff in west and central HMA, and significant interdecadal variability in central and east HMA. We also used the traditional Fourier Transform method to perform the power spectra analysis and detect the periodic oscillations of hydroclimatic time series, which shows consistency with the results obtained by the DWS method. Given the dominant role of precipitation in runoff variability in HMA, we further investigated the large-scale atmospheric drivers to explore the underlying mechanisms behind the spatial heterogeneity of hydroclimatic variability in HMA. The west-east pattern of runoff variability at interannual, interdecadal and multidecadal timescales coincides well with the location of convection anomalies generated by the atmospheric drivers. From the above results, it is thought that the space-time pattern of runoff in HMA identified in this study is credible and method-independent.

To check the potential influence of different supplies on the runoff variability in HMA, we estimated the runoff compositions by the SPHY model. However, there may have some uncertainties in the simulation of runoff compositions, which usually comes from the accuracy of forcing data, integration of necessary hydro-cryospheric processes and setting of sensitivity parameters (L. Zhang et al., 2013). In high mountain areas, the meteorological variables like precipitation and air temperature are characterized by vertical lapse rates, but it is not well represented by the observations of meteorological station mostly located in valleys (Q. Zhao et al., 2019). As discussed in Section 5.2.1, precipitation could be underestimated, which might lead to overestimation of the glacier-snow melt water (Lutz et al., 2014). For the runoff compositions obtained from the SPHY model, we have compared them with the previous studies using the isotope tracing method and digital filter method (Table S1 in Supporting

Information S1). Their similarity confirms the reliability of the runoff compositions estimation results by the SPHY model used in this study.

It is noted that this study was mainly focused on observational analysis, just as did at basin-scale worldwide in many related studies. In our future work, we will conduct empirical and physical model analysis by considering the dynamics of groundwater and glacier-snow meltwater, to verify the results in this study and improve the understanding of runoff variability and its drivers in HMA.

5.3. Runoff Nonstationary

During recent decades, hydroclimatic processes tend to be nonstationary under the global climate changes. Particularly, HMA has experienced a warming rate twice as much the global average, accelerating the glacier retreat and permafrost degradation. It motivates many researchers to investigate the response of runoff to changes in climate and cryosphere (Han et al., 2019; Jiang et al., 2022; J. Wang et al., 2021). It is found that there are significant shifts in hydrological regimes including the runoff magnitude, streamflow recession, precipitation-runoff relationship and water yield around 2000 (H. Li et al., 2022; X. Li et al., 2022; J. Wang et al., 2022), whereas the monotonic trend in runoff is not significant (as shown in our results).

In this study, we focused on the periodic oscillations of runoff at interannual, interdecadal and multidecadal timescales in HMA. However, we could not detect significant shifts in the periodic oscillations of precipitation and runoff during the period concerned. Actually, the instrumental records for several decades are usually insufficient to discuss the shifts in the periodic oscillations of hydroclimatic variables (Y. Yang et al., 2021). As a result, it's hard to say whether the shifts in hydroclimatic processes in HMA are natural variability or nonstationary behavior. Longer observations, or geological and biological proxies (Wu et al., 2022), are needed to further clarify the nonstationary variability of runoff in HMA, by considering together the influences of climate change and human activities (H. Li et al., 2022; X. Li et al., 2022; Lutz et al., 2022; Q. Zhang et al., 2023).

6. Conclusions

In this study, we identified the spatial and temporal variability of runoff in HMA, and examined the influences of climate conditions and catchment properties on the runoff variability. We find that the runoff in the west and central HMA shows a significant variability at the interannual and multidecadal timescales, but the interdecadal variability of runoff is more significant in central and east HMA. The runoff variability is mainly controlled by the variability in climate conditions, especially precipitation. Besides, the catchment properties, including the groundwater storage, soil moisture, and glacier-snow meltwater, appear to play important roles in the runoff variability by regulating the climate effects. In particular, the high contributions of glacier-snow meltwater would weaken the runoff variability at interannual and multidecadal timescales, buffering the runoff response to precipitation. It is concluded that both the climate conditions and catchment properties should be considered to understand the long-term variability in runoff and its spatial manifestation in HMA. Moreover, the space-time patterns in the runoff variability over HMA are driven by the ENSO, IPO, and AMO at the interannual, interdecadal, and multidecadal timescales, respectively.

Based on the improved understanding in the physical mechanisms of runoff variability in HMA, it is desirable to give reliable estimations and predictions the runoff variability, which could provide guidance for sustainable freshwater management and mitigation of water-related disasters in the region.

Data Availability Statement

The APHRODITE and CMA meteorological data sets (e.g., precipitation and temperature) are obtained at http://www.chikyu.ac.jp/precip/products.html (Yatagai et al., 2012) and http://data.cma.cn (Y. F. Zhao & Zhu, 2015), respectively. The SRTM DEM data set is provided at https://cgiarcsi.community/data/srtm-90m-digital-elevation-database-v4-1/ (Jarvis et al., 2008). The land use products can be accessed at https://www.resdc.cn/DOI/DOI.aspx?DOIID=54 (Xu et al., 2018). The soil properties from HWSD are available at https://www.fao.org/soils-portal/data-hub/soil-maps-and-databases/harmonized-world-soil-database-v12/en (Fischer et al., 2008). The ERA5 reanalysis data is accessed at https://doi.org/10.24381/cds.6860a573 (Hersbach et al., 2023). The sea surface temperature data from ERSSTv5 is provided by https://psl.noaa.gov/data/gridded/data.noaa.ersst.v5.html

(B. Huang et al., 2017). The climate indices are available at https://psl.noaa.gov/gcos_wgsp/Timeseries/ (Enfield et al., 2001; Mantua et al., 1997; Rayner et al., 2003). The streamflow observations are obtained from the Hydrology and Water Resources Bureau of Tibet Autonomous Region through a restricted use agreement per government regulations. Those interested in using the streamflow observation data need to follow the same procedure. The SPHY model codes can be accessed through the github repository at https://github.com/FutureWater/SPHY (Terink et al., 2015). Other processed data and codes in this study are available at https://doi.org/10.5281/zenodo.8023760 (Zhu et al., 2023a) and https://doi.org/10.5281/zenodo.8023394 (Zhu et al., 2023b), respectively.

Acknowledgments
The authors gratefully acknowledged the valuable comments and suggestions given by the Editors and reviewers on earlier versions, which led to significant improvements to the presentation of the work performed. This project was financially supported by the National Key Research and Development Program (No. 2019YFA0606903), the Strategic Priority Research Program of the Chinese Academy of Sciences (CAS) (No. XDA20060402), and the National Natural Science Foundation of China (Nos. 41971040, 91647110). The first author also thanked the support of China Scholarship Council.

References

Agarwal, A., Marwan, N., Rathinasamy, M., Merz, B., & Kurths, J. (2017). Multi-scale event synchronization analysis for unravelling climate processes: A wavelet-based approach. *Nonlinear Processes in Geophysics*, *24*(4), 599–611. https://doi.org/10.5194/npg-24-599-2017

Bachmair, S., & Weiler, M. (2012). Hillslope characteristics as controls of subsurface flow variability. *Hydrology and Earth System Sciences*, *16*(10), 3699–3715. https://doi.org/10.5194/hess-16-3699-2012

Berghuijs, W. R., & Woods, R. A. (2016). Correspondence: Space-time asymmetry undermines water yield assessment. *Nature Communications*, *7*(1), 1–2. https://doi.org/10.1038/ncomms11603

Budyko, M. I. (1974). *Climate and life*. Academic.

Carmona, A. M., Sivapalan, M., Yaeger, M. A., & Poveda, G. (2014). Regional patterns of interannual variability of catchment water balances across the continental US: A Budyko framework. *Water Resources Research*, *50*(12), 9177–9193. https://doi.org/10.1002/2014WR016013

Carrillo, G., Troch, P. A., Sivapalan, M., Wagener, T., Harman, C., & Sawicz, K. (2011). Catchment classification: Hydrological analysis of catchment behavior through process-based modeling along a climate gradient. *Hydrology and Earth System Sciences*, *15*(11), 3411–3430. https://doi.org/10.5194/hess-15-3411-2011

Cherchi, A., Alessandri, A., Masina, S., & Navarra, A. (2011). Effects of increased CO_2 levels on monsoon. *Climate Dynamics*, *37*(1–2), 83–101. https://doi.org/10.1007/s00382-010-0801-7

Cui, P., & Jia, Y. (2015). Mountain hazards in the Tibetan Plateau: Research status and prospects. *National Science Review*, *2*(4), 397–402. https://doi.org/10.1093/nsr/nwv061

Cuo, L., Li, N., Liu, Z., Ding, J., Liang, L., Zhang, Y., & Gong, T. (2019). Warming and human activities induced changes in the Yarlung Tsangpo basin of the Tibetan plateau and their influences on streamflow. *Journal of Hydrology: Regional Studies*, *25*, 100625. https://doi.org/10.1016/j.ejrh.2019.100625

Cuo, L., Zhang, Y., Zhu, F., & Liang, L. (2014). Characteristics and changes of streamflow on the Tibetan Plateau: A review. *Journal of Hydrology: Regional Studies*, *2*, 49–68. https://doi.org/10.1016/j.ejrh.2014.08.004

Curio, J., & Scherer, D. (2016). Seasonality and spatial variability of dynamic precipitation controls on the Tibetan Plateau. *Earth System Dynamics*, *7*(3), 767–782. https://doi.org/10.5194/esd-7-767-2016

Dilley, M. (2005). *Natural disaster hotspots: A global risk analysis* (Vol. 5). World Bank Publications. https://doi.org/10.1596/0-8213-5930-4

Dong, B., & Dai, A. (2015). The influence of the interdecadal Pacific oscillation on temperature and precipitation over the globe. *Climate Dynamics*, *45*(9), 2667–2681. https://doi.org/10.1007/s00382-015-2500-x

Dong, W., Lin, Y., Wright, J. S., Ming, Y., Xie, Y., Wang, B., et al. (2016). Summer rainfall over the southwestern Tibetan Plateau controlled by deep convection over the Indian subcontinent. *Nature Communications*, *7*(1), 10925. https://doi.org/10.1038/ncomms10925

Enfield, D. B., Mestas-Nuñez, A. M., & Trimble, P. J. (2001). The Atlantic multidecadal oscillation and its relation to rainfall and river flows in the continental US. *Geophysical Research Letters*, *28*(10), 2077–2080. https://doi.org/10.1029/2000GL012745

Fischer, G., Nachtergaele, F., Prieler, S., van Velthuizen, H. T., Verelst, L., & Wiberg, D. (2008). Global Agro-ecological Zones Assessment for Agriculture (GAEZ 2008) [Dataset]. IIASA and FAO. https://www.fao.org/soils-portal/data-hub/soil-maps-and-databases/harmonized-world-soil-database-v12/en/

Fu, B. P. (1981). On the calculation of the evaporation from land surface. *Scientia Atmospherica Sinica*, *5*(1), 23. https://cir.nii.ac.jp/crid/1371694364625911058

Gudmundsson, L., Tallaksen, L. M., Stahl, K., & Fleig, A. K. (2011). Low-frequency variability of European runoff. *Hydrology and Earth System Sciences*, *15*(9), 2853–2869. https://doi.org/10.5194/hess-15-2853-2011

Han, Z., Long, D., Fang, Y., Hou, A., & Hong, Y. (2019). Impacts of climate change and human activities on the flow regime of the dammed Lancang River in Southwest China. *Journal of Hydrology*, *570*, 96–105. https://doi.org/10.1016/j.jhydrol.2018.12.048

Hersbach, H., Bell, B., Berrisford, P., Biavati, G., Horányi, A., Muñoz Sabater, J., et al. (2023). ERA5 monthly averaged data on pressure levels from 1940 to present [Dataset]. Copernicus Climate Change Service (C3S) Climate Data Store (CDS). https://doi.org/10.24381/cds.6860a573

Horton, R. E. (1932). Drainage-basin characteristics. *Transactions - American Geophysical Union*, *13*(1), 350–361. https://doi.org/10.1029/TR013i001p00350

Hu, S., Wu, B., Zhou, T., & Yu, Y. (2022). Dominant anomalous circulation patterns of Tibetan Plateau summer climate generated by ENSO-forced and ENSO-independent teleconnections. *Journal of Climate*, *35*(5), 1679–1694. https://doi.org/10.1175/JCLI-D-21-0207.1

Hu, S., & Zhou, T. (2021). Skillful prediction of summer rainfall in the Tibetan Plateau on multiyear time scales. *Science Advances*, *7*(24), eabf9395. https://doi.org/10.1126/sciadv.abf9395

Hu, S., Zhou, T., & Wu, B. (2021). Impact of developing ENSO on Tibetan Plateau summer rainfall. *Journal of Climate*, *34*(9), 3385–3400. https://doi.org/10.1175/JCLI-D-20-0612.1

Hu, S., Zhou, T., & Wu, B. (2022). The physical processes dominating the impact of the summer North Atlantic Oscillation on the eastern Tibetan Plateau summer rainfall. *Journal of Climate*, *35*(23), 4077–4090. https://doi.org/10.1175/JCLI-D-21-0661.1

Huang, B., Thorne, P. W., Banzon, V. F., Boyer, T., Chepurin, G., Lawrimore, J. H., et al. (2017). NOAA extended reconstructed sea surface temperature (ERSST), version 5 [Dataset]. NOAA National Centers for Environmental Information, *30*(8179–8205), 25. https://psl.noaa.gov/data/gridded/data.noaa.ersst.v5.html

Huang, X., Zhou, T., Dai, A., Li, H., Li, C., Chen, X., et al. (2020). South Asian summer monsoon projections constrained by the interdecadal Pacific oscillation. *Science Advances*, *6*(11), eaay6546. https://doi.org/10.1126/sciadv.aay6546

Immerzeel, W. W., van Beek, L. P. H., & Bierkens, M. F. P. (2010). Climate change will affect the Asian water towers. *Science*, *328*(5984), 1382–1385. https://doi.org/10.1126/science.1183188

Immerzeel, W. W., Lutz, A. F., Andrade, M., Bahl, A., Biemans, H., Bolch, T., et al. (2020). Importance and vulnerability of the world's water towers. *Nature*, *577*(7790), 364–369. https://doi.org/10.1038/s41586-019-1822-y

Istanbulluoglu, E., Wang, T., Wright, O. M., & Lenters, J. D. (2012). Interpretation of hydrologic trends from a water balance perspective: The role of groundwater storage in the Budyko hypothesis. *Water Resources Research*, *48*(3). https://doi.org/10.1029/2010WR010100

Jarvis, A., Reuter, H. I., Nelson, A., & Guevara, E. (2008). Hole-filled SRTM for the globe Version 4, available from the CGIAR-CSI SRTM 90m Database [Dataset]. CGIAR-CSI, *15*(25–54), 5. https://cgiarcsi.community/data/srtm-90m-digital-elevation-database-v4-1/

Jiang, Y., Xu, Z., & Xiong, L. (2022). Runoff variation and response to precipitation on multi-spatial and temporal scales in the southern Tibetan Plateau. *Journal of Hydrology: Regional Studies*, *42*, 101157. https://doi.org/10.1016/j.ejrh.2022.101157

Khanal, S., Lutz, A. F., Kraaijenbrink, P. D. A., van den Hurk, B., Yao, T., & Immerzeel, W. W. (2021). Variable 21st century climate change response for rivers in High Mountain Asia at seasonal to decadal time scales. *Water Resources Research*, *57*(5), e2020WR029266. https://doi.org/10.1029/2020WR029266

Lai, H. W., Chen, H. W., Kukulies, J., Ou, T., & Chen, D. (2021). Regionalization of seasonal precipitation over the Tibetan Plateau and associated large-scale atmospheric systems. *Journal of Climate*, *34*(7), 2635–2651. https://doi.org/10.1175/JCLI-D-20-0521.1

Li, H., Shan, B., Liu, L., Wang, L., Koppa, A., Zhong, F., et al. (2022). Significant regime shifts in historical water yield in the Upper Brahmaputra River basin. *Hydrology and Earth System Sciences*, *26*(24), 6399–6412. https://doi.org/10.5194/hess-26-6399-2022

Li, T., Wang, B., Wu, B., Zhou, T., Chang, C. P., & Zhang, R. (2017). Theories on formation of an anomalous anticyclone in western North Pacific during El Niño: A review. *Journal of Meteorological Research*, *31*(6), 987–1006. https://doi.org/10.1007/s13351-017-7147-6

Li, X., Long, D., Scanlon, B. R., Mann, M. E., Li, X., Tian, F., et al. (2022). Climate change threatens terrestrial water storage over the Tibetan Plateau. *Nature Climate Change*, *12*(9), 801–807. https://doi.org/10.1038/s41558-022-01443-0

Liu, J., Zhang, Q., Feng, S., Gu, X., Singh, V. P., & Sun, P. (2019). Global attribution of runoff variance across multiple timescales. *Journal of Geophysical Research: Atmospheres*, *124*(24), 13962–13974. https://doi.org/10.1029/2019JD030539

Lutz, A. F., Immerzeel, W. W., Shrestha, A. B., & Bierkens, M. F. P. (2014). Consistent increase in High Asia's runoff due to increasing glacier melt and precipitation. *Nature Climate Change*, *4*(7), 587–592. https://doi.org/10.1038/nclimate2237

Lutz, A. F., Immerzeel, W. W., Siderius, C., Wijngaard, R. R., Nepal, S., Shrestha, A. B., et al. (2022). South Asian agriculture increasingly dependent on meltwater and groundwater. *Nature Climate Change*, *12*(6), 566–573. https://doi.org/10.1038/s41558-022-01355-z

Mantua, N. J., Hare, S. R., Zhang, Y., Wallace, J. M., & Francis, R. C. (1997). A Pacific interdecadal climate oscillation with impacts on salmon production. *Bulletin of the American Meteorological Society*, *78*(6), 1069–1080. https://doi.org/10.1175/1520-0477(1997)078%3C1069:APICOW%3E2.0.CO;2

Moore, I. D., Grayson, R. B., & Ladson, A. R. (1991). Digital terrain modelling: A review of hydrological, geomorphological, and biological applications. *Hydrological Processes*, *5*(1), 3–30. https://doi.org/10.1002/hyp.3360050103

Nippgen, F., McGlynn, B. L., Marshall, L. A., & Emanuel, R. E. (2011). Landscape structure and climate influences on hydrologic response. *Water Resources Research*, *47*(12). https://doi.org/10.1029/2011WR011161

Rayner, N. A. A., Parker, D. E., Horton, E. B., Folland, C. K., Alexander, L. V., Rowell, D. P., & Kaplan, A. (2003). Global analyses of sea surface temperature, sea ice, and night marine air temperature since the late nineteenth century. *Journal of Geophysical Research*, *108*(D14), 4407. https://doi.org/10.1029/2002JD002670

Rice, J. S., Emanuel, R. E., & Vose, J. M. (2016). The influence of watershed characteristics on spatial patterns of trends in annual scale streamflow variability in the continental US. *Journal of Hydrology*, *540*, 850–860. https://doi.org/10.1016/j.jhydrol.2016.07.006

Rice, J. S., Emanuel, R. E., Vose, J. M., & Nelson, S. A. (2015). Continental US streamflow trends from 1940 to 2009 and their relationships with watershed spatial characteristics. *Water Resources Research*, *51*(8), 6262–6275. https://doi.org/10.1002/2014WR016367

Rinderer, M., Van Meerveld, H. J., & Seibert, J. (2014). Topographic controls on shallow groundwater levels in a steep, prealpine catchment: When are the TWI assumptions valid? *Water Resources Research*, *50*(7), 6067–6080. https://doi.org/10.1002/2013WR015009

Sang, Y. F. (2012). A practical guide to discrete wavelet decomposition of hydrologic time series. *Water Resources Management*, *26*(11), 3345–3365. https://doi.org/10.1007/s11269-012-0075-4

Sang, Y. F., Singh, V. P., Gong, T., Xu, K., Sun, F., Liu, C., et al. (2016). Precipitation variability and response to changing climatic condition in the Yarlung Tsangpo River basin, China. *Journal of Geophysical Research: Atmospheres*, *121*(15), 8820–8831. https://doi.org/10.1002/2016JD025370

Sang, Y. F., Sivakumar, B., & Zhang, Y. (2020). Is there an underestimation of long-term variability of streamflow across the continental United States? *Journal of Hydrology*, *581*, 124365. https://doi.org/10.1016/j.jhydrol.2019.124365

Sang, Y. F., Sivakumar, B., & Zhu, Y. (2021). Uniform discrete wavelet spectrum for detection of hydrologic variability at multiple timescales. *Journal of Hydro-Environment Research*, *35*, 31–37. https://doi.org/10.1016/j.jher.2021.01.005

Sang, Y. F., Sun, F., Singh, V. P., Xie, P., & Sun, J. (2018). A discrete wavelet spectrum approach for identifying non-monotonic trends in hydroclimate data. *Hydrology and Earth System Sciences*, *22*(1), 757–766. https://doi.org/10.5194/hess-22-757-2018

Sankarasubramanian, A., & Vogel, R. M. (2003). Hydroclimatology of the continental United States. *Geophysical Research Letters*, *30*(7). https://doi.org/10.1029/2002GL015937

Sawicz, K., Wagener, T., Sivapalan, M., Troch, P. A., & Carrillo, G. (2011). Catchment classification: Empirical analysis of hydrologic similarity based on catchment function in the eastern USA. *Hydrology and Earth System Sciences*, *15*(9), 2895–2911. https://doi.org/10.5194/hess-15-2895-2011

Strang, G., & Nguyen, T. (1996). *Wavelets and filter banks*. SIAM.

Sun, J., Yang, K., Guo, W., Wang, Y., He, J., & Lu, H. (2020). Why has the inner Tibetan Plateau become wetter since the mid-1990s? *Journal of Climate*, *33*(19), 8507–8522. https://doi.org/10.1175/JCLI-D-19-0471.1

Takaya, K., & Nakamura, H. (2001). A formulation of a phase-independent wave-activity flux for stationary and migratory quasi-geostrophic eddies on a zonally varying basic flow. *Journal of the Atmospheric Sciences*, *58*(6), 608–627. https://doi.org/10.1175/1520-0469(2001)058<0608:AFOAPI>2.0.CO;2

Tan, H., Chen, X., Shi, D., Rao, W., Liu, J., Liu, J., et al. (2021). Base flow in the Yarlungzangbo River, Tibet, maintained by the isotopically-depleted precipitation and groundwater discharge. *Science of The Total Environment*, *759*, 143510. https://doi.org/10.1016/j.scitotenv.2020.143510

Tang, Q., Lan, C., Su, F., Liu, X., Sun, H., Ding, J., et al. (2019). Streamflow change on the Qinghai-Tibet Plateau and its impacts. *Chinese Science Bulletin*, *64*(27), 2807–2821. https://doi.org/10.1360/TB-2019-0141

Terink, W., Lutz, A. F., Simons, G. W. H., Immerzeel, W. W., & Droogers, P. (2015). SPHY v2. 0: Spatial processes in hydrology. *Geoscientific Model Development*, *8*(7), 2009–2034. https://doi.org/10.5194/gmd-8-2009-2015

Tong, K., Su, F., Yang, D., Zhang, L., & Hao, Z. (2014). Tibetan Plateau precipitation as depicted by gauge observations, reanalysis and satellite retrievals. *International Journal of Climatology*, *34*(2), 265–285. https://doi.org/10.1002/joc.3682

Wang, A., & Zeng, X. (2012). Evaluation of multireanalysis products with in situ observations over the Tibetan Plateau. *Journal of Geophysical Research*, *117*(D5). https://doi.org/10.1029/2011JD016553
Wang, B., Wu, R., & Li, T. I. M. (2003). Atmosphere–warm ocean interaction and its impacts on Asian–Australian monsoon variation. *Journal of Climate*, *16*(8), 1195–1211. https://doi.org/10.1175/1520-0442(2003)16<1195:AOIAII>2.0.CO;2
Wang, B., Xiang, B., Li, J., Webster, P. J., Rajeevan, M. N., Liu, J., & Ha, K. J. (2015). Rethinking Indian monsoon rainfall prediction in the context of recent global warming. *Nature Communications*, *6*(1), 1–9. https://doi.org/10.1038/ncomms8154
Wang, H., Sankarasubramanian, A., & Ranjithan, R. S. (2015). Understanding the low-frequency variability in hydroclimatic attributes over the southeastern US. *Journal of Hydrology*, *521*, 170–181. https://doi.org/10.1016/j.jhydrol.2014.09.081
Wang, J., Chen, X., Gao, M., Hu, Q., & Liu, J. (2022). Changes in nonlinearity and stability of streamflow recession characteristics under climate warming in a large glaciated basin of the Tibetan Plateau. *Hydrology and Earth System Sciences*, *26*(14), 3901–3920. https://doi.org/10.5194/hess-26-3901-2022
Wang, J., Chen, X., Liu, J., & Hu, Q. (2021). Changes of precipitation-runoff relationship induced by climate variation in a large glaciated basin of the Tibetan Plateau. *Journal of Geophysical Research: Atmospheres*, *126*(21), e2020JD034367. https://doi.org/10.1029/2020JD034367
Wang, L., Yao, T., Chai, C., Cuo, L., Su, F., Zhang, F., et al. (2021). TP-River: Monitoring and quantifying total river runoff from the Third Pole. *Bulletin of the American Meteorological Society*, *102*(5), E948–E965. https://doi.org/10.1175/BAMS-D-20-0207.1
Wang, P. X., Wang, B., Cheng, H., Fasullo, J., Guo, Z., Kiefer, T., & Liu, Z. (2017). The global monsoon across time scales: Mechanisms and outstanding issues. *Earth-Science Reviews*, *174*, 84–121. https://doi.org/10.1016/j.earscirev.2017.07.006
Wang, Y., Wang, L., Zhou, J., Yao, T., Yang, W., Zhong, X., et al. (2021). Vanishing glaciers at southeast Tibetan Plateau have not offset the declining runoff at Yarlung Zangbo. *Geophysical Research Letters*, *48*(21), e2021GL094651. https://doi.org/10.1029/2021GL094651
Wang, Z., Duan, A., Yang, S., & Ullah, K. (2017). Atmospheric moisture budget and its regulation on the variability of summer precipitation over the Tibetan Plateau. *Journal of Geophysical Research: Atmospheres*, *122*(2), 614–630. https://doi.org/10.1002/2016JD025515
Wickerhauser, M. V. (1996). *Adapted wavelet analysis: From theory to software*. CRC Press.
Wu, Y., Long, D., Lall, U., Scanlon, B. R., Tian, F., Fu, X., et al. (2022). Reconstructed eight-century streamflow in the Tibetan Plateau reveals contrasting regional variability and strong nonstationarity. *Nature Communications*, *13*(1), 6416. https://doi.org/10.1038/s41467-022-34221-9
Xu, X., Liu, J., Zhang, S., Li, R., Yan, C., & Wu, S. (2018). Landuse dataset in China (1980-2015) [Dataset]. Chinese Academy of Sciences Resource and Environmental Science Data Center. https://www.resdc.cn/DOI/DOI.aspx?DOIID=54
Xu, X., Liu, W., Scanlon, B. R., Zhang, L., & Pan, M. (2013). Local and global factors controlling water-energy balances within the Budyko framework. *Geophysical Research Letters*, *40*(23), 6123–6129. https://doi.org/10.1002/2013GL058324
Yang, H., Yang, D., Lei, Z., & Sun, F. (2008). New analytical derivation of the mean annual water-energy balance equation. *Water Resources Research*, *44*(3). https://doi.org/10.1029/2007WR006135
Yang, L., Li, K., Shen, Y., & Tian, F. (2022). Flood seasonality over the Third Pole region modulated by upper level moisture transport. *Earth's Future*, *10*(9), e2022EF002828. https://doi.org/10.1029/2022EF002828
Yang, Y., Roderick, M. L., Yang, D., Wang, Z., Ruan, F., McVicar, T. R., et al. (2021). Streamflow stationarity in a changing world. *Environmental Research Letters*, *16*(6), 064096. https://doi.org/10.1088/1748-9326/ac08c1
Yao, T., Masson-Delmotte, V., Gao, J., Yu, W., Yang, X., Risi, C., et al. (2013). A review of climatic controls on δ18O in precipitation over the Tibetan Plateau: Observations and simulations. *Reviews of Geophysics*, *51*(4), 525–548. https://doi.org/10.1002/rog.20023
Yao, T., Thompson, L., Yang, W., Yu, W., Gao, Y., Guo, X., et al. (2012). Different glacier status with atmospheric circulations in Tibetan Plateau and surroundings. *Nature Climate Change*, *2*(9), 663–667. https://doi.org/10.1038/nclimate1580
Yao, T., Xue, Y., Chen, D., Chen, F., Thompson, L., Cui, P., et al. (2019). Recent third pole's rapid warming accompanies cryospheric melt and water cycle intensification and interactions between monsoon and environment: Multidisciplinary approach with observations, modeling, and analysis. *Bulletin of the American Meteorological Society*, *100*(3), 423–444. https://doi.org/10.1175/BAMS-D-17-0057.1
Yao, Y., Zheng, C., Andrews, C. B., Scanlon, B. R., Kuang, X., Zeng, Z., et al. (2021). Role of groundwater in sustaining northern Himalayan rivers. *Geophysical Research Letters*, *48*(10), e2020GL092354. https://doi.org/10.1029/2020GL092354
Yatagai, A., Kamiguchi, K., Arakawa, O., Hamada, A., Yasutomi, N., & Kitoh, A. (2012). APHRODITE: Constructing a long-term daily gridded precipitation dataset for Asia based on a dense network of rain gauges. *Bulletin of the American Meteorological Society*, *93*(9), 1401–1415. https://doi.org/10.1175/BAMS-D-11-00122.1
Zhang, L., Dawes, W. R., & Walker, G. R. (2001). Response of mean annual evapotranspiration to vegetation changes at catchment scale. *Water Resources Research*, *37*(3), 701–708. https://doi.org/10.1029/2000WR900325
Zhang, L., Su, F., Yang, D., Hao, Z., & Tong, K. (2013). Discharge regime and simulation for the upstream of major rivers over Tibetan Plateau. *Journal of Geophysical Research: Atmospheres*, *118*(15), 8500–8518. https://doi.org/10.1002/jgrd.50665
Zhang, Q., Shen, Z., Pokhrel, Y., Farinotti, D., Singh, V. P., Xu, C. Y., et al. (2023). Oceanic climate changes threaten the sustainability of Asia's water tower. *Nature*, *615*(7950), 87–93. https://doi.org/10.1038/s41586-022-05643-8
Zhang, T., Wang, T., Krinner, G., Wang, X., Gasser, T., Peng, S., et al. (2019). The weakening relationship between Eurasian spring snow cover and Indian summer monsoon rainfall. *Science Advances*, *5*(3), eaau8932. https://doi.org/10.1126/sciadv.aau8932
Zhang, X., Dong, Q., Cheng, L., & Xia, J. (2019). A Budyko-based framework for quantifying the impacts of aridity index and other factors on annual runoff. *Journal of Hydrology*, *579*, 124224. https://doi.org/10.1016/j.jhydrol.2019.124224
Zhao, Q., Ding, Y., Wang, J., Gao, H., Zhang, S., Zhao, C., et al. (2019). Projecting climate change impacts on hydrological processes on the Tibetan Plateau with model calibration against the glacier inventory data and observed streamflow. *Journal of Hydrology*, *573*, 60–81. https://doi.org/10.1016/j.jhydrol.2019.03.043
Zhao, Y., & Zhou, T. (2021). Interannual variability of precipitation recycle ratio over the Tibetan Plateau. *Journal of Geophysical Research: Atmospheres*, *126*(2), e2020JD033733. https://doi.org/10.1029/2020JD033733
Zhao, Y. F., & Zhu, J. (2015). Assessing quality of grid daily precipitation datasets in China in recent 50 years. *Plateau Meteorology*, *34*(1), 50–58. https://doi.org/10.7522/j.issn.1000-0534.2013.00141
Zhu, Y., & Sang, Y. (2018). Spatial variability in the seasonal distribution of precipitation on the Tibetan Plateau. *Progress in Geography*, *37*(11), 1533–1544. https://doi.org/10.18306/dlkxjz.2018.11.009
Zhu, Y., Sang, Y. F., Chen, D., Sivakumar, B., & Li, D. (2020). Effects of the South Asian summer monsoon anomaly on interannual variations in precipitation over the South-Central Tibetan Plateau. *Environmental Research Letters*, *15*(12), 124067. https://doi.org/10.1088/1748-9326/abc71b
Zhu, Y., Sang, Y. F., Wang, B., Lutz, A. F., Hu, S., Chen, D., & Singh, V. P. (2023a). Supporting data to Heterogeneity in spatiotemporal variability of High Mountain Asia's runoff and its underlying mechanisms [Dataset]. Zenodo. https://doi.org/10.5281/zenodo.8023760
Zhu, Y., Sang, Y. F., Wang, B., Lutz, A. F., Hu, S., Chen, D., & Singh, V. P. (2023b). Supporting codes to Heterogeneity in spatiotemporal variability of High Mountain Asia's runoff and its underlying mechanisms [Software]. Zenodo. https://doi.org/10.5281/zenodo.8023394